Supplement of Atmos. Chem. Phys., 26, 16957–16983, 2026
https://doi.org/10.5194/acp-26-16957-2026-supplement
© Author(s) 2026. CC BY 4.0 License.



Atmospheric Chemistry and Physics
Open Access
EGU

Supplement of

Ice-nucleating properties of α-pinene- and limonene-derived secondary organic aerosol under cirrus conditions

Christopher N. Rapp et al.

Correspondence to: Daniel J. Cziczo (djcziczo@purdue.edu)

The copyright of individual parts of the supplement might differ from the article licence.

S1 Methodology

S1.1 Particle classification thresholds

Table S1: Initial SPIN OPC parameters used to perform supervised SVM classification where x is the 1 second averaged particle property with respect to each class.

Class	δ_{SPIN}	$\log_{10}(\mathrm{I_{size}})$	$\mathrm{S_{liq}}$
Aerosol	$x < 0.16$	$x \leq 0.125$	-
Droplet	$0.16 \leq x \leq 0.35$	$0.35 \leq x$	$1 \leq x$
Ice	$0.4 \leq x$	$0.4 \leq x$	-
Water Uptake	$x < 0.35$	$0.125 \leq x \leq 0.4$	-

S1.2 Application of the multimodal curve fitting algorithm

Modes were determined using a multimodal curve fitting algorithm (Rapp et al., 2026). The output returned a list of modes with lognormal parameters i.e. number concentration (N), geometric mean diameter ($\overline{D_{\mathrm{pg}}}$), and geometric standard deviation (σ_g). Only modes with less than 5% min-max normalized root mean square error were retained and over 90% of all particle variance was explained by the fit. Size distribution data 1.5 hours before the start of SPIN experiments was isolated and clustered using an unsupervised K-means algorithm with 8 centroids. Data was grouped by cluster and averaged to obtain a reference $\overline{D_{pg}}$ and σ_g. The underlying physical structure of the particle size distribution was then partitioned into seven groups: Self-nucleated, Singlet (z = 4), Singlet (z = 3), Singlet (z = 2), Singlet, Doublet, and Triplet. As experiments were always conducted with 300 nm size selected sulfate seed particles prior to the PAM-OFR, classification was structured as detailed in Table S2.

Table S2 – Reference diameters for assignment from K-means output of multimodal fitting

Mode	Reference D_{pg} (nm)	Assignment range (nm)
Singlet (z = 4)	115	100–130
Singlet (z = 3)	150	125–175
Singlet (z = 2)	190	160–220
Singlet	300	245–355
Doublet	500	430–570
Triplet	650	580–720

Given that up to 10 modes could be returned by the multimodal algorithm during highly transient self-nucleation, duplicated mode assignments were made for the 8 centroid K-means algorithm. These were averaged using an occurrence weighted mean for each mode. The primary dataset corresponding to SPIN measurement was then assigned particle modes using the determined weighted mode scheme.

The modal assignment was then used to calculate the surface area of each mode per SEMS measurement (~ 2 minutes) using the second moment of a lognormal particle size distribution (Eq. S1) where $\overline{D_{\mathrm{pg}}}$ is expressed in units of m.

$$\mathrm{SA} = N\pi\overline{D_{\mathrm{pg}}}^{2}\exp\left[2\left(\ln\sigma_g\right)\right] \quad \text{(S1)}$$

As multiple self-nucleation modes could exist simultaneously, the surface areas of all similar particle modes were summed at each time interval. The fraction that each fitted mode contributes to surface area was then calculated by dividing by the total fitted surface area per scan. These fractions were then multiplied by the total binned surface area from the SEMS. The mean ratio between fitted surface area and SEMS measured surface area was 0.985 ± 0.098 (where error is defined as one standard deviation from the mean), indicating high accuracy in both fitting and modal attribution.

Coating thickness was derived using the multimodal output by comparing SEMS measurements where only seeds were present. We note that seeds were only introduced after several hours of flushing maximum oxidants through the PAM-OFR and an absence of any detected self-nucleated particles on the SEMS. The characteristic seed distribution was assigned modes using the same weighted mean reference data and averaged to obtain a set of initial diameters for the following classes: Singlet (z = 4), Singlet (z = 3), Singlet (z = 2), Singlet, Doublet, and Triplet. The diameters of same-class modes were then subtracted from these initial diameters and divided by two to retrieve coating thickness. No interpolation was made for any surface area or coating estimate to prevent biasing any descriptive statistics.

Number fraction ratios and concentrations were obtained similarly, with a primary focus given to the singlet to doublet ratio and fraction of organic particles above each IN diameter threshold.

S1.3 Derivation of the organic glass transition temperature.

S1.3.1 Conversion of VIA thermograms to effective saturation concentrations

The volatility distributions of the secondary organic aerosol (SOA) were determined using the Vaporization Inlet for Aerosols coupled with a Vocus chemical ionization mass spectrometer operated in the NH_4^+ reagent-ion mode (VIA–Vocus-CIMS). The analysis followed the thermogram method described by Niu et al., (2025). For each assigned organic ion *i*, the background-corrected thermogram was fitted using the sigmoidal function (Eq. S2):

$$I_{i(T)} = \frac{a_i}{1 + \exp\left(-\frac{T - T_{50,i}}{b_i}\right)} \quad \text{(S2)}$$

where $I_{i(T)}$ is the ion signal at VIA temperature T, a_i is the fitted maximum signal, b_i describes the steepness of the thermogram, and $T_{50,i}$ is the temperature at which the fitted ion signal reaches 50% of its maximum value. The calibration relationship between T_{50} and C* (Eq. S3) from Niu et al. (2025) was adopted here:

$$log_{10} C_i^* = -19 + 6.9 \times 10^3 T_{50,i}^{-1} \quad S3$$

where $T_{50,i}$ is expressed in kelvin and C_i^* is expressed in μm/m^3. The published calibration was constructed using cis-pinonic acid, glutaric acid, adipic acid, azelaic acid, sebacic acid, dodecanedioic acid, and polyethylene glycol 400 (PEG-8) as volatility standards.

The detected ions were primarily ammonium adducts. The NH_4^+ adduct was removed during molecular-formula assignment. Therefore, the carbon, hydrogen, oxygen, and sulfur atom numbers and the molar masses used below refer to the neutral organic compounds. The calibration above provides an effective saturation concentration for a compound in the SOA matrix. Following Niu et al. (2025), C_i^* was approximated as the pure-compound saturation concentration C_i^0 when applying the glass-transition-temperature parameterization by assuming an activity coefficient of unity.

S1.3.2 Glass-transition temperatures derived from volatility

The glass-transition temperature of each detected compound was estimated from its effective saturation concentration using the semiempirical relationship developed by Zhang et al. (2019):

$$T_{g,i} = 480.07 - \frac{54395}{(log_{10}\left(\frac{RT_{ref}C_i^*}{\xi_i M_i}\right) - 7.7929)^2 + 116.49} \quad (S4)$$

where $T_{g,i}$ is in K, R=8.2×10^{-5} m^3 atm mol^{-1} K^{-1}, T_{ref} = 298 K, M_i is the molar mass of the neutral organic compound, and ξ_i is the activity coefficient, which was assumed to be unity for all compounds.

S1.3.3 Glass-transition temperatures derived from molecular formulas

As a complementary method, the glass-transition temperature of each detected compound was parameterized directly from the numbers of carbon (n_C), hydrogen (n_H), oxygen n_O, and sulfur atoms (n_S) in its assigned neutral molecular formula following Li et al. (2020):

$$T_{g,\mathrm{org}} = (n_C^0 + \ln(n_C))b_C + \ln(n_H)\, b_H + \ln(n_C)\ln(n_H)\, b_{CH} + \ln(n_O)\, b_O + \ln(n_C)\ln(n_O)\, b_{CO} \quad S5$$

values of the coefficients n_C^0, b_C, b_H, b_{CH}, b_O, and b_{CO} are 1.96, 61.99, −113.33, 28.74, 0, and 0 for CH compounds and 12.13, 10.95, −41.82, 21.61, 118.96, and −24.38 for CHO compounds. For sulfur containing compounds, the modified equation shown below was used:

$$T_{g,\mathrm{org}} = (n_C^0 + \ln(n_C))b_C + \ln(n_O)\, b_O + \ln(n_S)\, b_S + \ln(n_C)\ln(n_O)\, b_{CO} + \ln(n_C)\ln(n_S)\, b_{CS} + \ln(n_O)\ln(n_S)\, b_{OS} \quad S6$$

Values of the coefficients n_C^0, b_C, b_O, b_{CO}, b_{CS}, and b_{OS} are 1.12, 68.41, 64.95, 35.77, −12.32, −9.85, and 13.80 respectively. All $T_{g,org}$ values calculated here are expressed in K.

S1.3.4 Calculation of the dry bulk-organic glass-transition temperature

The compound-specific glass-transition temperatures were combined using the Gordon–Taylor mixing relationship. For a dry mixture of organic compounds, the Gordon–Taylor constant was assumed to be unity. Because compound-specific Vocus-CIMS sensitivities were unavailable, the relative ion-signal fractions were used as proxies for the relative contributions of the detected compounds. Under these assumptions, the dry bulk-organic glass-transition temperature (Eq. S7) reduces to a linearly weighted average (Eq. 8) of signal intensity:

$$T_{g,org} = \sum_i w_i T_{g,i} \quad S7$$

where I_i is the signal intensity for compound i.

$$w_i = \frac{I_i}{\sum_i I_i} \quad S8$$

S1.3.5 Propagated uncertainties for T_g derivation

The uncertainty reported for the thermogram-derived T_g was calculated by propagating the error of the calibration relationship between T_{50} and C* from Niu et al. (2025) and the sigmoid fitting of the thermograms. Several additional sources of uncertainty could not be quantitatively constrained, including uncertainty in the Zhang et al. (2019) volatility–$T_{g,org}$ parameterization and compound-specific response factors in Vocus-CIMS due to the lack of authentic SOA standards.

DeRieux et al. (2018) reported an approximate 68% prediction interval of ±21 K for predictions of individual compounds and was adopted here. Zhang et al. (2019) did not report a transferable uncertainty range for the volatility-based relationship. Similarly, Li et al. (2020) evaluated the CHOS parameterization using correlation and relative-error statistics but did not provide a universal prediction interval.

Consequently, the uncertainties reported for the thermogram-derived estimates should be interpreted as propagated measurement precision. The total uncertainty associated with both $T_{g,org}$ estimation methods is expected to be larger because the systematic and parameterization uncertainties listed above could not be quantitatively constrained.

S2 Results

S2.1 PALMS-NG

S2.1.1 Fraction of uncoated particles

The fraction of uncoated particles was determined using PALMS-NG. First, we defined the total number of particles as those passing quality assurance / quality control (QA/QC) within the sampling time frames corresponding to each particle (see Table S3).

Table S3 – Summary of PALMS-NG analysis to determine the fraction of uncoated particles corresponding to each seed particle and gas-phase precursor.

Date	Seed Particle	Gas-phase precursor	Total Number	Uncoated	Fraction Uncoated (%)
2023-10-09	AS	α-pinene	3360	1	0.03
2023-10-10	PNS	α-pinene	350	3	0.86
2023-10-16	AS	limonene	733	8	1.09
2023-10-17	PNS	limonene	1267	6	0.47

We then totaled areas corresponding to reference organic *m/z* values, where areas are fractional values of the integrated ion intensity normalized to the sum of total ion intensity in each ion mode (e.g. positive or negative). The positive ions were observed at *m/z* 36, 39, 43, 45, 59 corresponding to the fragments C_3^+, $C_3H_3^+$, $C_3H_7/C_2H_3O/CH_3CO^+$, $COOH^+$, CH_2COOH^+. The negative ions were observed at *m/z* 24, 25, 26, 45, and 59 corresponding to the fragments C_2^-, C_2H^-, $C_2H_2^-$, $COOH^-$, CH_2COOH^-, respectively. A particle was considered uncoated if the sum of the areas corresponding to the organic fragments defined above were zero in both the positive and negative mode.

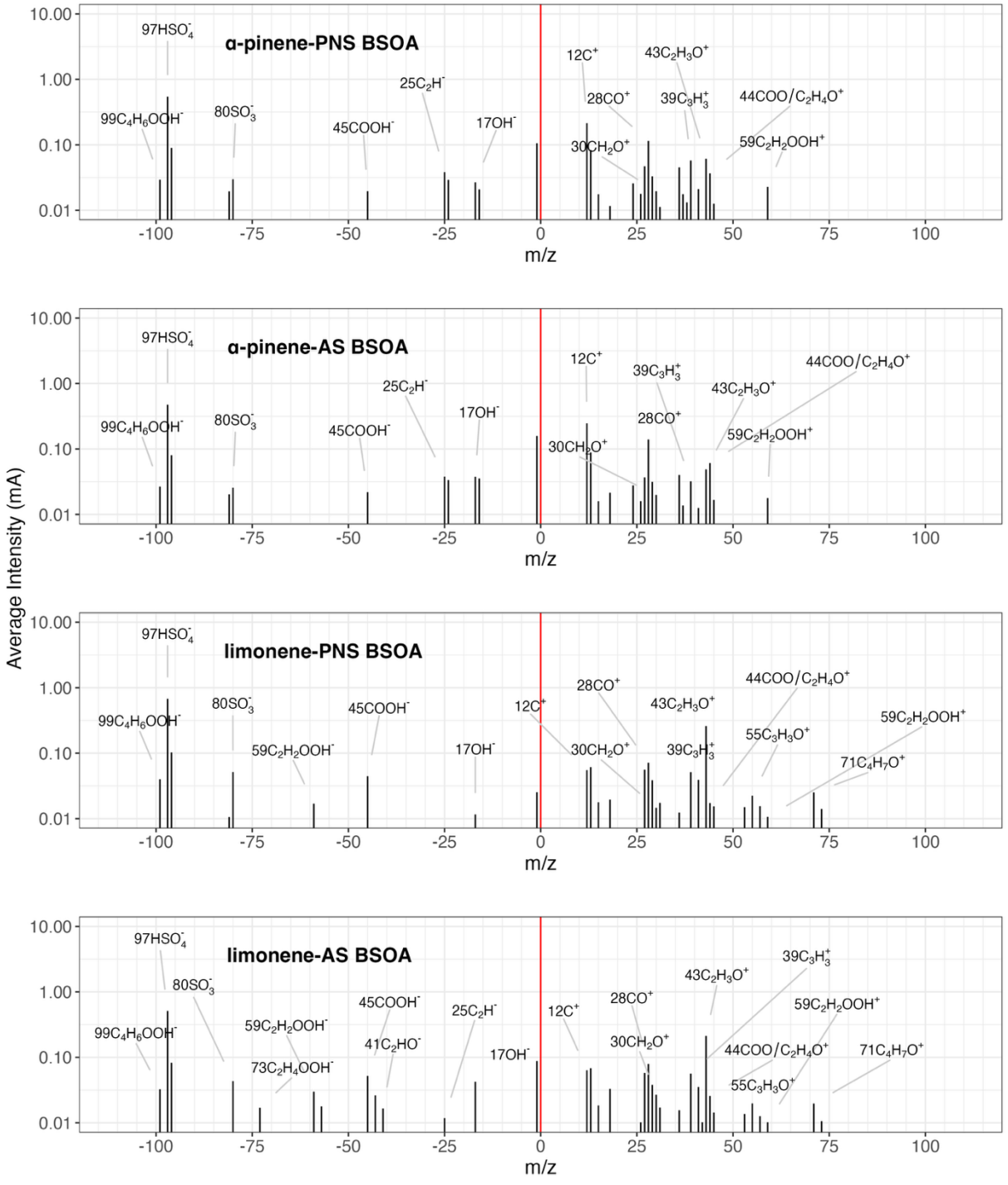
α-pinene-PNS BSOA
α-pinene-AS BSOA
limonene-PNS BSOA
limonene-AS BSOA
Average Intensity (mA)
m/z
10.00
1.00
0.10
0.01
-100
-75
-50
-25
0
25
50
75
100
97HSO4-
99C4H6OOH-
80SO3-
45COOH-
25C2H-
17OH-
12C+
43C2H3O+
28CO+
39C3H3+
44COO/C2H4O+
30CH2O+
59C2H2OOH+
59C2H2OOH-
55C3H3O+
71C4H7O+
41C2HO-
73C2H4OOH-

Figure S1 – Averaged mass spectra for each precursor-seed combination as labeled.

Spectra are limited to the singlet mode. Aerosol generation conditions correspond to Table 1. Spectra are plotted in log scale to accommodate the six orders of magnitude in dynamic range for PALMS-NG. Both positive and negative ions are shown and separated by the red line centered at *m/z* = 0. Known PALMS specific ion fragments are labeled as cataloged or previously identified in upper tropospheric measurements (Froyd et al., 2009; Murphy et al., 2006). The following ion fragments are unique to limonene BSOA: -59 *m/z* ($C_2H_2OOH^-$), +55 *m/z* ($C_3H_3O^+$), and +71 *m/z* ($C_4H_7O^+$). For α-pinene BSOA, +12 *m/z* (C^+) was the strongest positive ion fragment followed by +28 *m/z* (CO^+), with comparable intensities for +39 ($C_3H_3^+$) and +43 ($C_2H_3O^+$) *m/z*. No unique ion fragments were identified for α-pinene. A primary difference between α-pinene and limonene BSOA was the positive ion fragment ratio of 39:43, with seed specific ratios of (AS 0.66, PNS 0.94) and (AS 0.27, PNS 0.20) respectively.

S2.2 Vocus-CIMS

Table S4 – Chemical formulas of organosulfate compounds detected in coating experiments using VIA-Vocus-CIMS

(amu)	α-Pinene–AS BSOA	α-Pinene–PNS BSOA	Limonene–AS BSOA	Limonene–PNS BSOA
388	–	–	–	$C_{17}H_{24}O_6S_2$
374	–	–	–	$C_{12}H_{22}O_9S_2$
332	–	–	–	$C_{15}H_{24}O_4S_2$
320	–	–	–	$C_{11}H_{12}O_9S$
312	–	–	$C_{15}H_{20}O_5S$	–
298	$C_{13}H_{14}O_6S$	–	–	–
265	–	$C_8H_9O_8S$	–	–
246	–	–	–	$C_9H_{10}O_6S$
244	–	–	$C_8H_{20}O_6S$	–
240	$C_8H_{16}O_6S$	$C_8H_{16}O_6S$	$C_8H_{16}O_6S$	–
238	–	–	–	$C_9H_{18}O_5S$
234	–	–	$C_{10}H_{18}O_4S$; $C_{11}H_{22}O_3S$	–
226	–	–	–	$C_8H_{18}O_5S$
196	–	–	$C_{10}H_{12}O_2S$	$C_6H_{12}O_5S$
166	–	–	–	$C_6H_{14}O_3S$
162	–	–	–	$C_7H_{14}O_2S$
148	–	–	–	$C_6H_{12}O_2S$

S2.3 Multimodal particle size distributions (MPSDs)

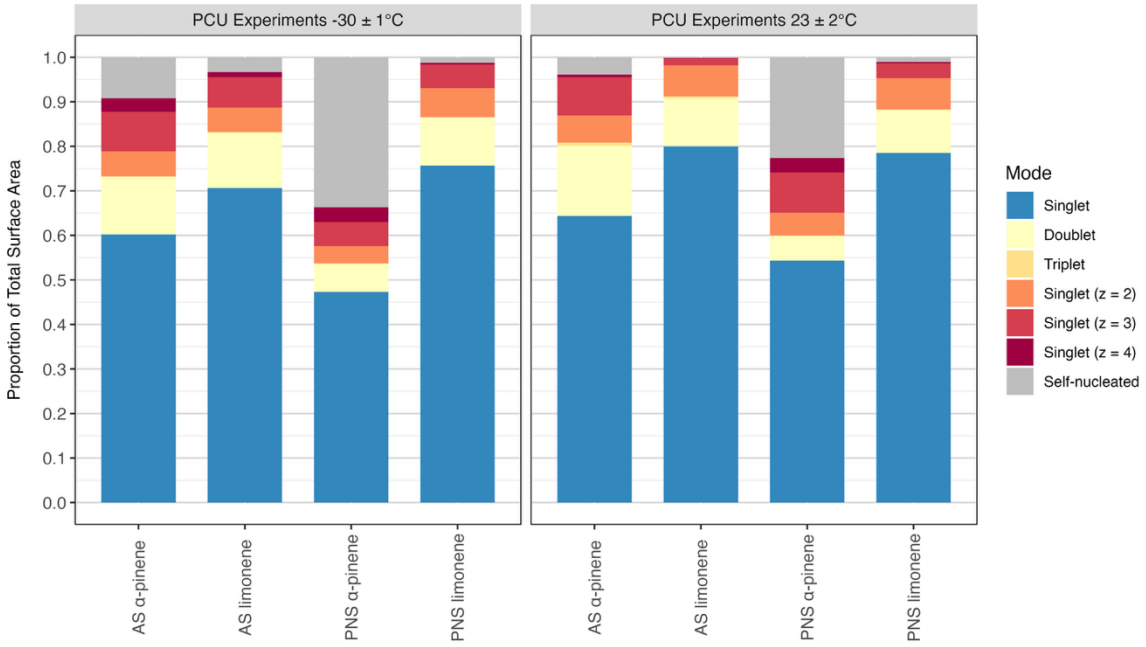

Figure S2 – Surface area contributions of modes decomposed from multimodal particle size distributions measured by the SEMS.

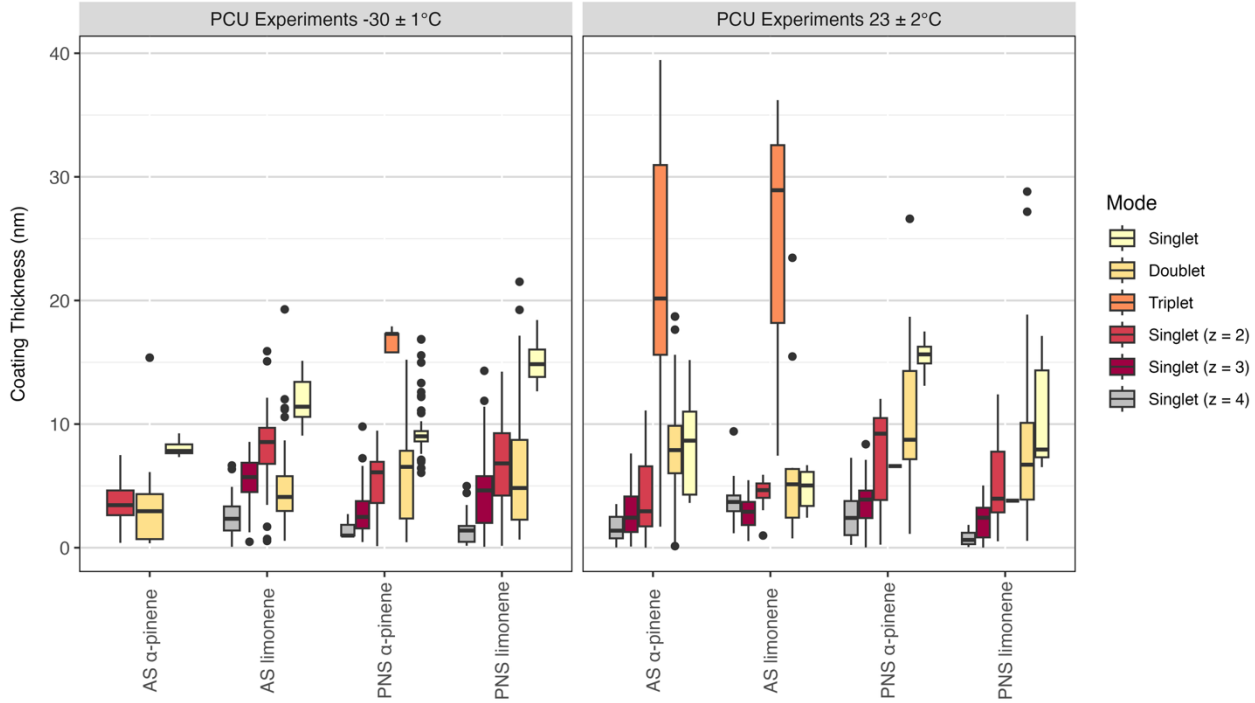

Figure S3 – Coating thickness per mode as determined using initial seed diameters and subtracting these from tracked modes throughout the temporal PSD for each experiment.

S2.4 SPectrometer for Ice Nucleation (SPIN)

Table S5 – A summary of all thermodynamic onsets and corresponding experimental parameters. From left to right: seed particle composition, gas-phase precursor for BSOA generation, SPIN-OPC classification for particle type, number of observations for a given onset, 0.5% AF onset S_{ice}, onset temperature, geometric mean diameter of the primary particle mode, geometric standard deviation of the primary particle mode, CPC particle concentration larger than 100 nm, BSOA coating thickness when applicable, PCU temperature, PCU RH, PCU inlet RH, percentage of particles that were self-nucleated, and percentage of singlet to doublet particles. Note that the the PNS limonene experiment without a PCU measurement was conducted at room temperature.

Seed	Precursor	Class	Obs.	Onset S_{ice}	Onset temperature (°C)	D_{pg} (nm)	σ_g	Coating thickness (nm)	CPC (n cm^{-3})	PCU temperature (°C)	PCU RH (%)	PCU inlet RH (%)	Self-nucleated organic (%)	Singlet to doublet (%)
AS	Seed Only	Ice	3132	1.34 ± 0.08	-44.8 ± 0.4	288.0 ± 1.1	1.08	-	7526	24.3 ± 1.0	0 ± 5	0 ± 5	-	94 ± 7.32
AS	Seed Only	Ice	1846	1.36 ± 0.08	-39.8 ± 0.4	286.0 ± 0.7	1.08	-	7690	24.7 ± 1.0	0 ± 5	0 ± 5	-	95 ± 7.24
AS	Seed Only	Ice	455	1.53 ± 0.10	-34.7 ± 0.5	283.4 ± 0.9	1.08	-	8560	24.8 ± 1.0	0 ± 5	0 ± 5	-	94 ± 6.54
AS	Seed Only	Droplet Breakthrough	308	1.54 ± 0.10	-34.7 ± 0.5	283.4 ± 0.9	1.08	-	8560	24.8 ± 1.0	0 ± 5	0 ± 5	-	94 ± 6.54
AS	α-pinene	Ice	1080	1.49 ± 0.10	-45.2 ± 0.4	310.9 ± 5.7	1.1	8.3 ± 2.9	17811	23.3 ± 1.0	0 ± 5	0 ± 5	1 ± 0	91 ± 5.37
AS	α-pinene	Ice	1290	1.44 ± 0.08	-44.9 ± 0.4	316.4 ± 0.5	1.1	7.7 ± 0.3	44390	-29.8 ± 1.1	-	0 ± 5	12 ± 1	91 ± 6.06
AS	α-pinene	Ice	658	1.56 ± 0.10	-40.3 ± 0.4	302.2 ± 0.5	1.09	4 ± 0.2	9746	22.1 ± 1.0	0 ± 5	0 ± 5	0 ± 0	93 ± 6.53
AS	α-pinene	Ice	1115	1.46 ± 0.09	-40.2 ± 0.4	317.3 ± 4.1	1.11	11.6 ± 2.1	24479	22.0 ± 1.0	0 ± 5	0 ± 5	5 ± 0	90 ± 5.98
AS	α-pinene	Ice	1056	1.41 ± 0.09	-39.9 ± 0.4	318.0 ± 1.1	1.1	8.5 ± 0.5	46124	-29.8 ± 1.1	-	0 ± 5	11 ± 1	90 ± 5.78
AS	α-pinene	Droplet Breakthrough	108	1.55 ± 0.10	-40.4 ± 0.5	302.2 ± 0.5	1.09	4 ± 0.2	9746	22.1 ± 1.0	0 ± 5	0 ± 5	0 ± 0	93 ± 6.53
AS	α-pinene	Droplet Breakthrough	566	1.61 ± 0.11	-35.2 ± 0.5	313.6 ± 4.1	1.1	9.7 ± 2.1	52685	21.5 ± 1.0	0 ± 5	0 ± 5	4 ± 0	91 ± 5.33
AS	α-pinene	Water Uptake	279	1.48 ± 0.09	-45.2 ± 0.4	310.9 ± 5.7	1.1	8.3 ± 2.9	17811	23.3 ± 1.0	0 ± 5	0 ± 5	1 ± 0	91 ± 5.37
AS	α-pinene	Water Uptake	169	1.48 ± 0.09	-45.1 ± 0.4	316.4 ± 0.5	1.1	7.7 ± 0.3	44390	-29.8 ± 1.1	-	0 ± 5	12 ± 1	91 ± 6.06
AS	α-pinene	Water Uptake	181	1.48 ± 0.09	-40.4 ± 0.4	302.2 ± 0.5	1.09	4 ± 0.2	9746	22.1 ± 1.0	0 ± 5	0 ± 5	0 ± 0	93 ± 6.53
AS	α-pinene	Water Uptake	122	1.41 ± 0.08	-40.1 ± 0.4	317.3 ± 4.1	1.11	11.6 ± 2.1	24479	22.0 ± 1.0	0 ± 5	0 ± 5	5 ± 0	90 ± 5.98
AS	α-pinene	Water Uptake	326	1.32 ± 0.07	-39.9 ± 0.4	318.0 ± 1.1	1.1	8.5 ± 0.5	46124	-29.8 ± 1.1	-	0 ± 5	11 ± 1	90 ± 5.78
AS	limonene	Ice	1547	1.46 ± 0.09	-44.8 ± 0.4	314.4 ± 2.8	1.1	4.8 ± 1.4	19636	24.3 ± 1.0	0 ± 5	0 ± 5	0 ± 0	92 ± 5.00
AS	limonene	Ice	2181	1.36 ± 0.08	-44.7 ± 0.4	318.2 ± 2.1	1.1	10.7 ± 1.0	26916	-30.8 ± 1.1	-	0 ± 5	3 ± 0	92 ± 6.41
AS	limonene	Ice	1204	1.34 ± 0.07	-39.6 ± 0.4	324.3 ± 1.2	1.11	13.8 ± 0.6	29638	-30.5 ± 1.1	-	0 ± 5	2 ± 0	91 ± 5.28

PNS	Seed Only	Ice	1518	1.47 ± 0.10	-44.4 ± 0.5	296.5 ± 0.7	1.0 8	-	5947	24.3 ± 1.0	0 ± 5	0 ± 5	-	93 ± 8.63
PNS	Seed Only	Ice	905	1.50 ± 0.10	-39.5 ± 0.5	297.5 ± 0.8	1.0 8	-	5521	23.6 ± 1.0	0 ± 5	0 ± 5	-	94 ± 8.79
PNS	Seed Only	Droplet Breakthrough	593	1.54 ± 0.11	-34.4 ± 0.5	299.2 ± 1.1	1.0 8	-	5451	23.6 ± 1.0	0 ± 5	1 ± 5	-	94 ± 9.17
PNS	α-pinene	Ice	1313	1.47 ± 0.09	-44.9 ± 0.4	327.7 ± 2.2	1.1 3	15.1 ± 1.1	52616	20.5 ± 1.0	0 ± 5	0 ± 5	38 ± 3	90 ± 5.03
PNS	α-pinene	Ice	1313	1.47 ± 0.09	-45.0 ± 0.4	318.2 ± 1.0	1.1 1	9 ± 0.5	52082	-29.9 ± 1.1	-	0 ± 5	23 ± 2	91 ± 6.34
PNS	α-pinene	Ice	1198	1.41 ± 0.09	-39.8 ± 0.4	329.5 ± 1.5	1.1 3	15.9 ± 0.7	48366	23.3 ± 1.0	0 ± 5	0 ± 5	19 ± 2	93 ± 5.69
PNS	α-pinene	Ice	1259	1.39 ± 0.08	-39.7 ± 0.4	321.0 ± 6.9	1.1 1	10.4 ± 3.5	104945	-29.7 ± 1.1	-	0 ± 5	52 ± 6	91 ± 5.36
PNS	α-pinene	Water Uptake	426	1.45 ± 0.09	-45.0 ± 0.4	318.2 ± 1.0	1.1 1	9 ± 0.5	52082	-29.9 ± 1.1	-	0 ± 5	23 ± 2	91 ± 6.34
PNS	α-pinene	Water Uptake	212	1.37 ± 0.08	-40.1 ± 0.4	329.5 ± 1.5	1.1 3	15.9 ± 0.7	48366	23.3 ± 1.0	0 ± 5	0 ± 5	19 ± 2	93 ± 5.69
PNS	α-pinene	Water Uptake	288	1.31 ± 0.07	-40.0 ± 0.4	321.0 ± 6.9	1.1 1	10.4 ± 3.5	104945	-29.7 ± 1.1	-	0 ± 5	52 ± 6	91 ± 5.36
PNS	α-pinene	Water Uptake	322	1.26 ± 0.07	-34.8 ± 0.4	319.4 ± 6.0	1.1 1	9.6 ± 3.0	90807	-29.4 ± 1.1	-	0 ± 5	37 ± 2	92 ± 7.97
PNS	limonene	Ice	1889	1.37 ± 0.08	-44.7 ± 0.4	310.6 ± 1.7	1.0 9	7.7 ± 0.9	12309	-	-	-	0 ± 0	95 ± 13.80
PNS	limonene	Ice	1987	1.43 ± 0.08	-44.7 ± 0.4	325.4 ± 2.3	1.1 2	15.6 ± 1.1	21783	-31.6 ± 1.1	-	0 ± 5	0 ± 0	93 ± 8.17
PNS	limonene	Ice	1210	1.40 ± 0.08	-39.7 ± 0.4	325.1 ± 4.4	1.1 1	15 ± 2.2	23009	24.8 ± 1.0	0 ± 5	0 ± 5	2 ± 0	91 ± 5.27
PNS	limonene	Ice	1084	1.38 ± 0.08	-39.8 ± 0.4	322.2 ± 1.9	1.1 1	14 ± 0.9	20057	-30.9 ± 1.1	-	0 ± 5	0 ± 0	92 ± 8.32
PNS	limonene	Droplet Breakthrough	222	1.61 ± 0.11	-34.8 ± 0.5	324.7 ± 3.1	1.1 1	15.3 ± 1.5	23384	-30.8 ± 1.1	-	0 ± 5	0 ± 0	91 ± 4.61
-	α-pinene	Ice	1164	1.48 ± 0.09	-44.8 ± 0.4	87.0 ± 10.8	1.3 8	-	44710	24.0 ± 1.1	0 ± 5	0 ± 5	-	-
-	α-pinene	Ice	524	1.44 ± 0.09	-44.7 ± 0.4	88.3 ± 3.6	1.6 1	-	73167	-30.8 ± 1.1	-	0 ± 5	-	-
-	α-pinene	Ice	1013	1.40 ± 0.08	-40.0 ± 0.4	91.0 ± 8.1	1.3 6	-	35408	22.4 ± 1.1	0 ± 5	0 ± 5	-	-
-	α-pinene	Ice	1010	1.41 ± 0.09	-39.7 ± 0.4	87.3 ± 5.8	1.6 3	-	68677	-30.3 ± 1.1	-	0 ± 5	-	-
-	α-pinene	Droplet Breakthrough	650	1.48 ± 0.10	-34.8 ± 0.5	90.3 ± 7.8	1.3 1	-	40746	22.0 ± 1.1	0 ± 5	0 ± 5	-	-
-	α-pinene	Water Uptake	475	1.41 ± 0.09	-44.8 ± 0.4	87.0 ± 10.8	1.3 8	-	44710	24.0 ± 1.1	0 ± 5	0 ± 5	-	-
-	α-pinene	Water Uptake	790	1.26 ± 0.07	-39.8 ± 0.4	91.0 ± 8.1	1.3 6	-	35408	22.4 ± 1.1	0 ± 5	0 ± 5	-	-
-	α-pinene	Water Uptake	126	1.41 ± 0.08	-39.9 ± 0.4	87.3 ± 5.8	1.6 3	-	68677	-30.3 ± 1.1	-	0 ± 5	-	-
-	α-pinene	Water Uptake	518	1.26 ± 0.07	-34.8 ± 0.4	90.3 ± 7.8	1.3 1	-	40746	22.0 ± 1.1	0 ± 5	0 ± 5	-	-

-	limonene	Ice	2564	1.28 ± 0.07	-44.8 ± 0.3	68.4 ± 1.8	1.72	-	64460	24.0 ± 1.0	0 ± 5	0 ± 5	-	-
-	limonene	Ice	2196	1.31 ± 0.07	-44.7 ± 0.4	83.1 ± 1.5	1.78	-	68182	-30.2 ± 1.1	-	0 ± 5	-	-
-	limonene	Ice	1593	1.29 ± 0.07	-39.7 ± 0.4	72.0 ± 6.2	1.65	-	68778	23.8 ± 1.0	0 ± 5	0 ± 5	-	-
-	limonene	Ice	1502	1.27 ± 0.07	-39.8 ± 0.3	88.7 ± 2.0	1.76	-	65986	-30.3 ± 1.1	-	0 ± 5	-	-

170

Table S6 – A summary of background ice counts corresponding to the experiments presented in this study. The fraction of backgrounds contributing to the total number of ice particles per experiment is represented by the relative percentage. Note that high percentages corresponding to low ice counts are due to droplet breakthrough for experiments at -35°C

Seed	Precursor	PCU temperature (°C)	Lamina setpoint (°C)	Total Backgrounds ($n\ cm^{-3}$)	Total Ice ($n\ cm^{-3}$)	Percentage (%)
AS	Seed Only	23±2	-45	0	433440	0
AS	Seed Only	23±2	-40	1	226870	0
AS	Seed Only	23±2	-35	8	201043	0
AS	α-pinene	23±2	-45	1	263650	0
AS	α-pinene	23±2	-40	97	552265	0.02
AS	α-pinene	23±2	-35	3	23144	0.01
AS	α-pinene	-30±1	-45	268	336690	0.08
AS	α-pinene	-30±1	-40	216	304531	0.07
AS	limonene	23±2	-45	0	206808	0
AS	limonene	-30±1	-45	2	318722	0
AS	limonene	-30±1	-40	244	178060	0.14
PNS	Seed Only	23±2	-45	0	132200	0
PNS	Seed Only	23±2	-40	108	63674	0.17
PNS	Seed Only	23±2	-35	10	44	23.61
PNS	α-pinene	23±2	-45	0	176271	0
PNS	α-pinene	23±2	-40	3	327629	0
PNS	α-pinene	-30±1	-45	2	364605	0
PNS	α-pinene	-30±1	-40	6	365151	0
PNS	α-pinene	-30±1	-35	7	19487	0.04
PNS	limonene	23±2	-45	0	239159	0
PNS	limonene	23±2	-40	0	144172	0
PNS	limonene	-30±1	-45	0	306652	0
PNS	limonene	-30±1	-40	400	151042	0.26
PNS	limonene	-30±1	-35	108	17721	0.61
Self-Nucleated	α-pinene	-30±1	-45	1	177045	0
Self-Nucleated	α-pinene	-30±1	-40	19	311277	0.01
Self-Nucleated	α-pinene	23±2	-45	28	305349	0.01
Self-Nucleated	α-pinene	23±2	-40	14	291661	0
Self-Nucleated	α-pinene	23±2	-35	19	706	2.64
Self-Nucleated	limonene	23±2	-45	1	391516	0
Self-Nucleated	limonene	23±2	-40	1	245746	0
Self-Nucleated	limonene	-30±1	-45	1	339661	0
Self-Nucleated	limonene	-30±1	-40	2	238809	0

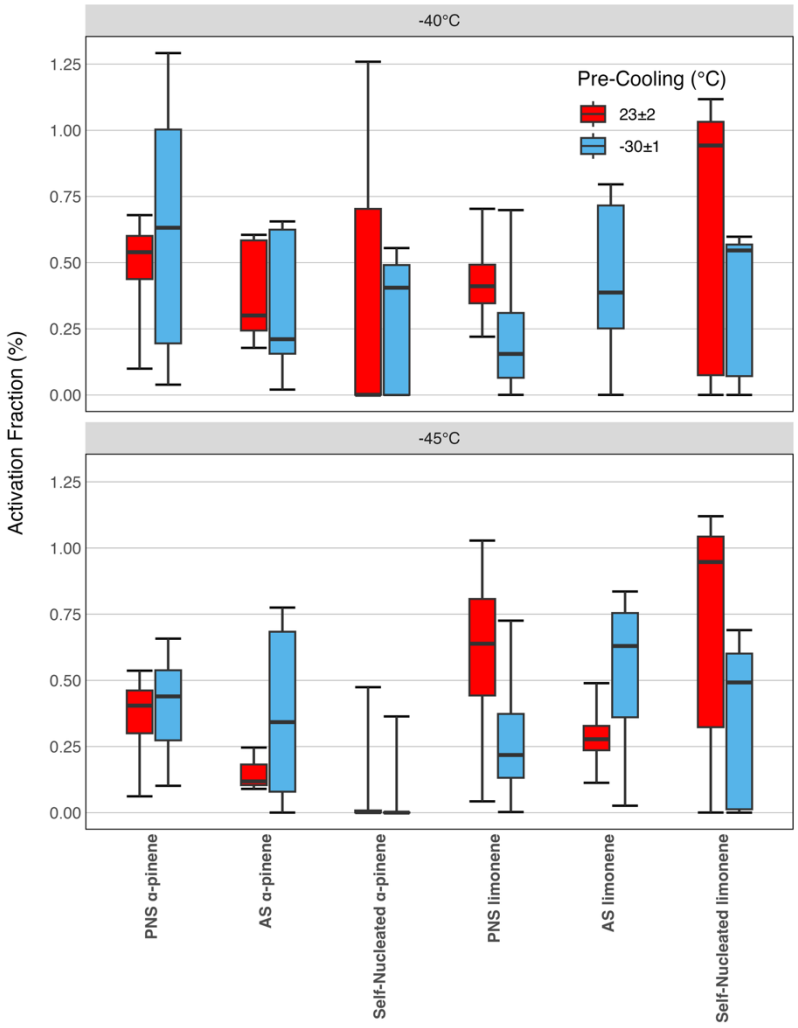

Figure S4 – Boxplot of heterogeneous AFs for each experiment without any smoothing or filtering as described in Sect. 2.6.3. Colors indicate the average pre-cooling temperature of the experiment. Panels are labeled by the average lamina temperature for the experiment. Whiskers are the min and maximum AF for each experiment without any outlier removal to accommodate the bias of AF values of 0 for much of each experiment until critical S_{ice} was reached.

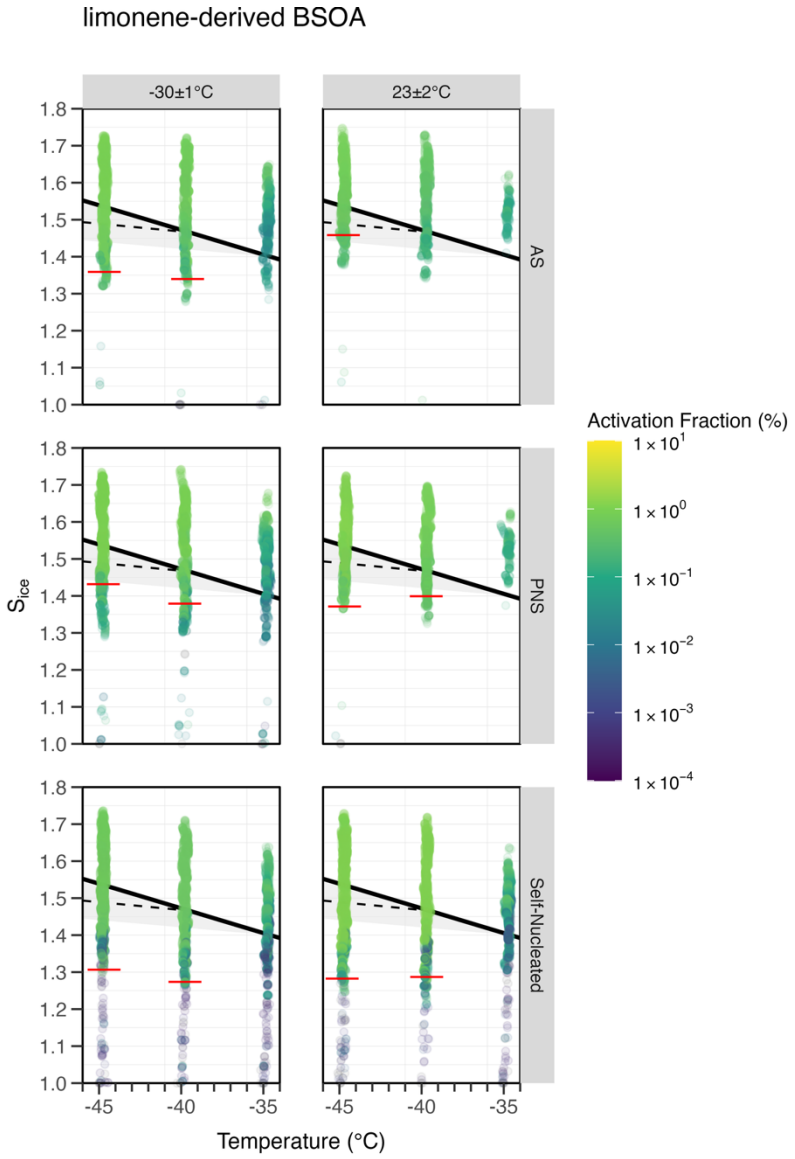

Figure S5 – Activated fractions of limonene-derived BSOA as a function of temperature and S_{ice}. Panel labels indicate pre-cooling temperature (top) or whether a seed was present (right). In each panel, solid black line represents water saturation, dashed black line is the homogeneous freezing threshold of 100 nm diameter solution droplets as defined by (Koop et al., 2000), with uncertainty in water activity (a_w) of ±2.5% represented by the gray shaded region (Koop, 2004). Red horizontal lines are the 0.5% ice onsets reported.

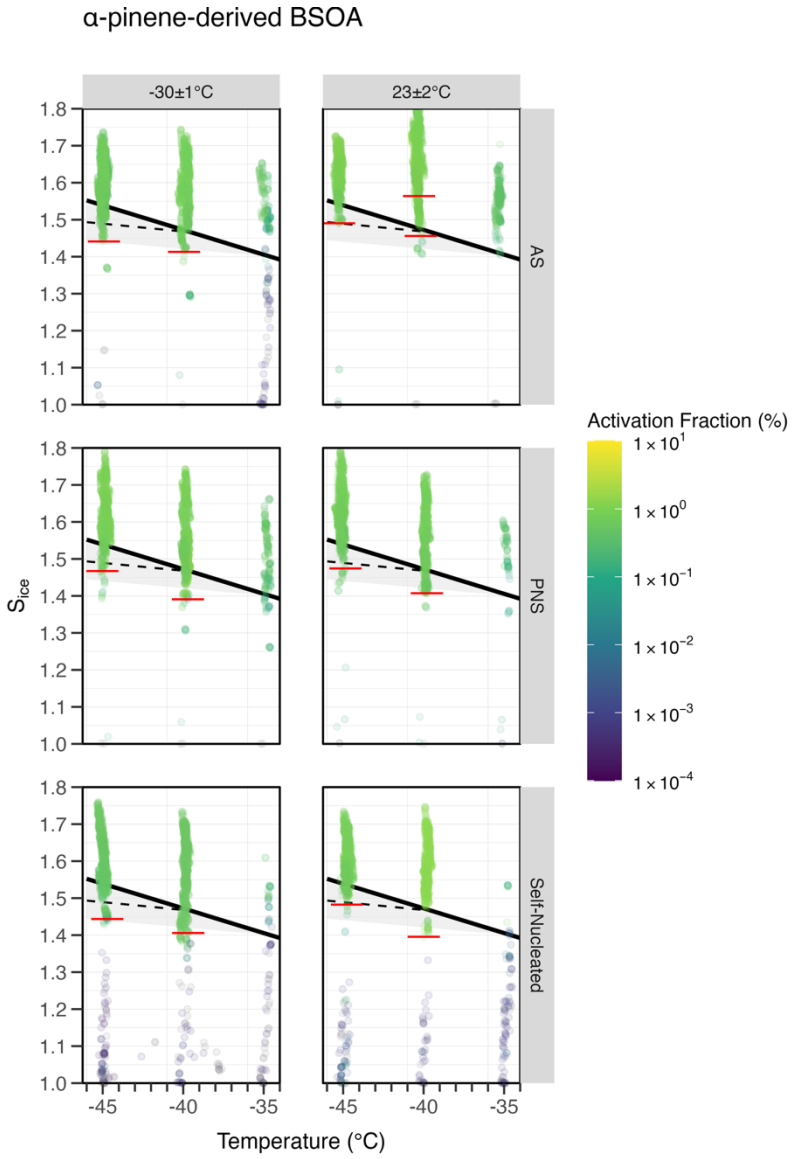

Figure S6 – Activated fractions of α-pinene-derived BSOA as a function of temperature and S_{ice}. Panel structure is identical to Figure S5.

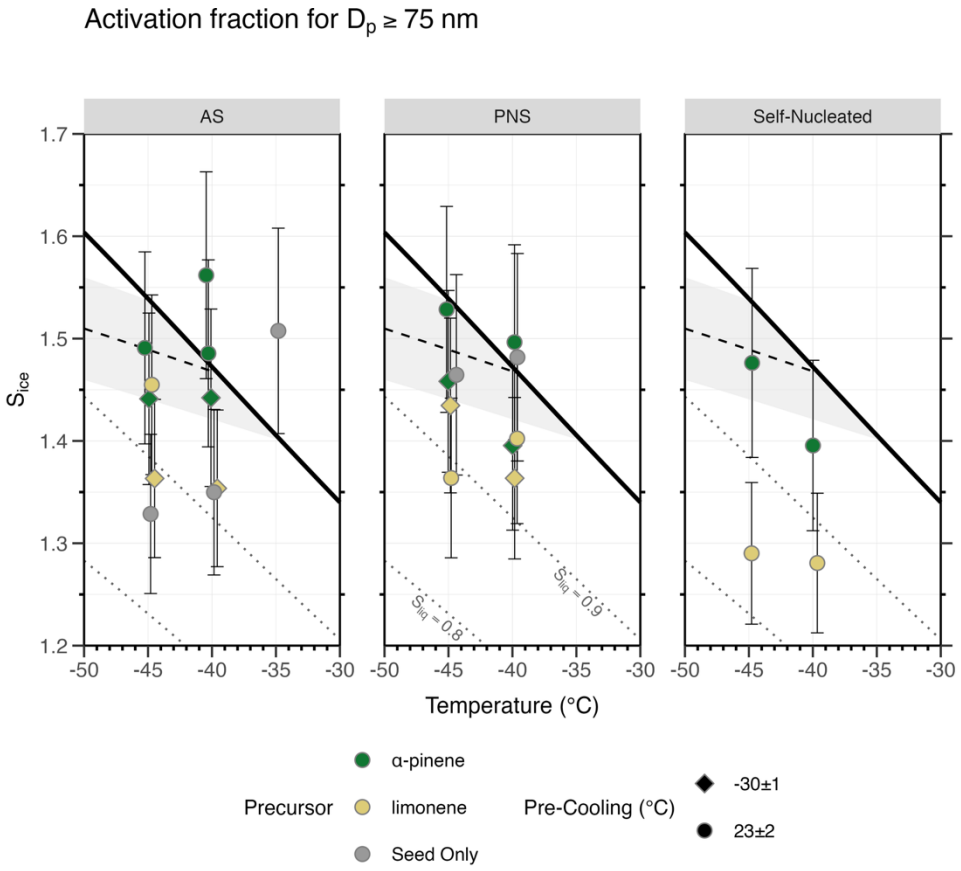

Figure S7 – Summary of thermodynamic onset conditions (T and S_{ice}) for an activation fraction of 0.5% of particles larger than 75 nm for all experiments conducted. Panels are separated and labelled according to sulfate seed particle or whether only self-nucleated particles were present. Colors indicate the precursor VOC used in generating BSOA or if bare seed particles were examined. Shapes indicate average pre-cooling temperature. Vertical error bars indicate the uncertainty in S_{ice} at onset of freezing. Shape width represents error in lamina temperature. Solid black line is water saturation i.e. $S_{liq} = 1$ with dotted black lines representing constant S_{liq} ratios. Dashed black line is the homogeneous freezing threshold of 100 nm diameter solution droplets as defined by (Koop et al., 2000), with uncertainty in water activity (a_w) of ±2.5% represented by the gray shaded region (Koop, 2004).

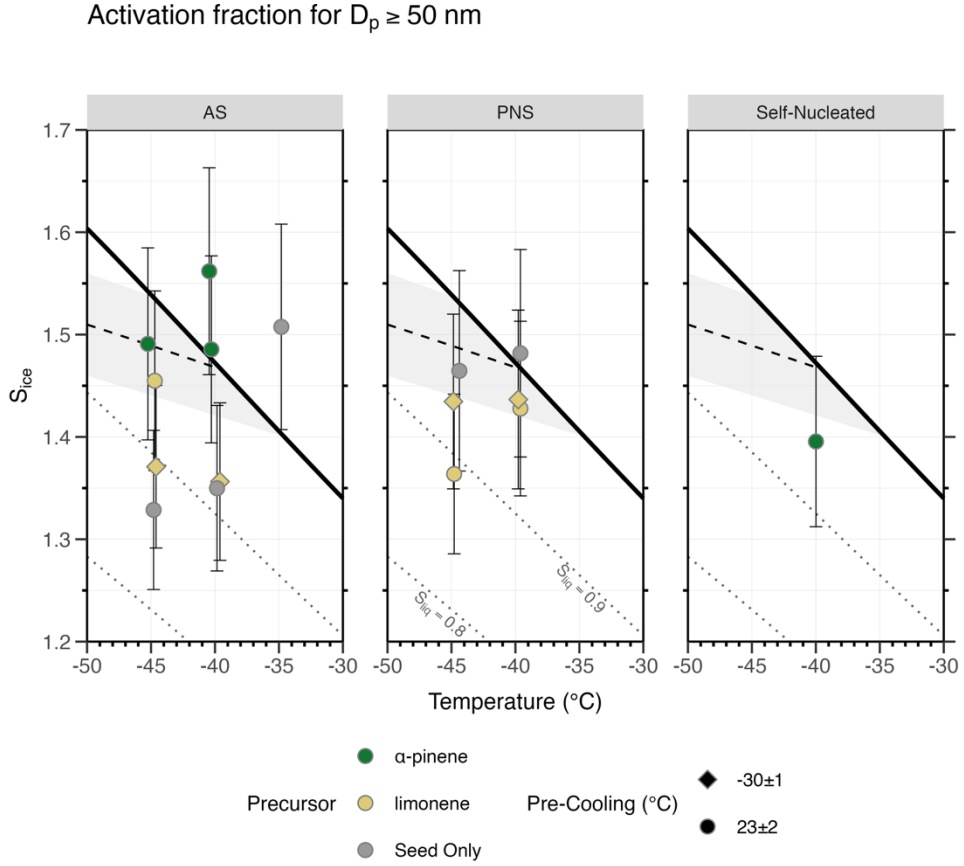

205

Figure S8 – Activated fractions of α-pinene-derived BSOA as a function of temperature and S_{ice}. Panel structure is identical to Fig. S7.

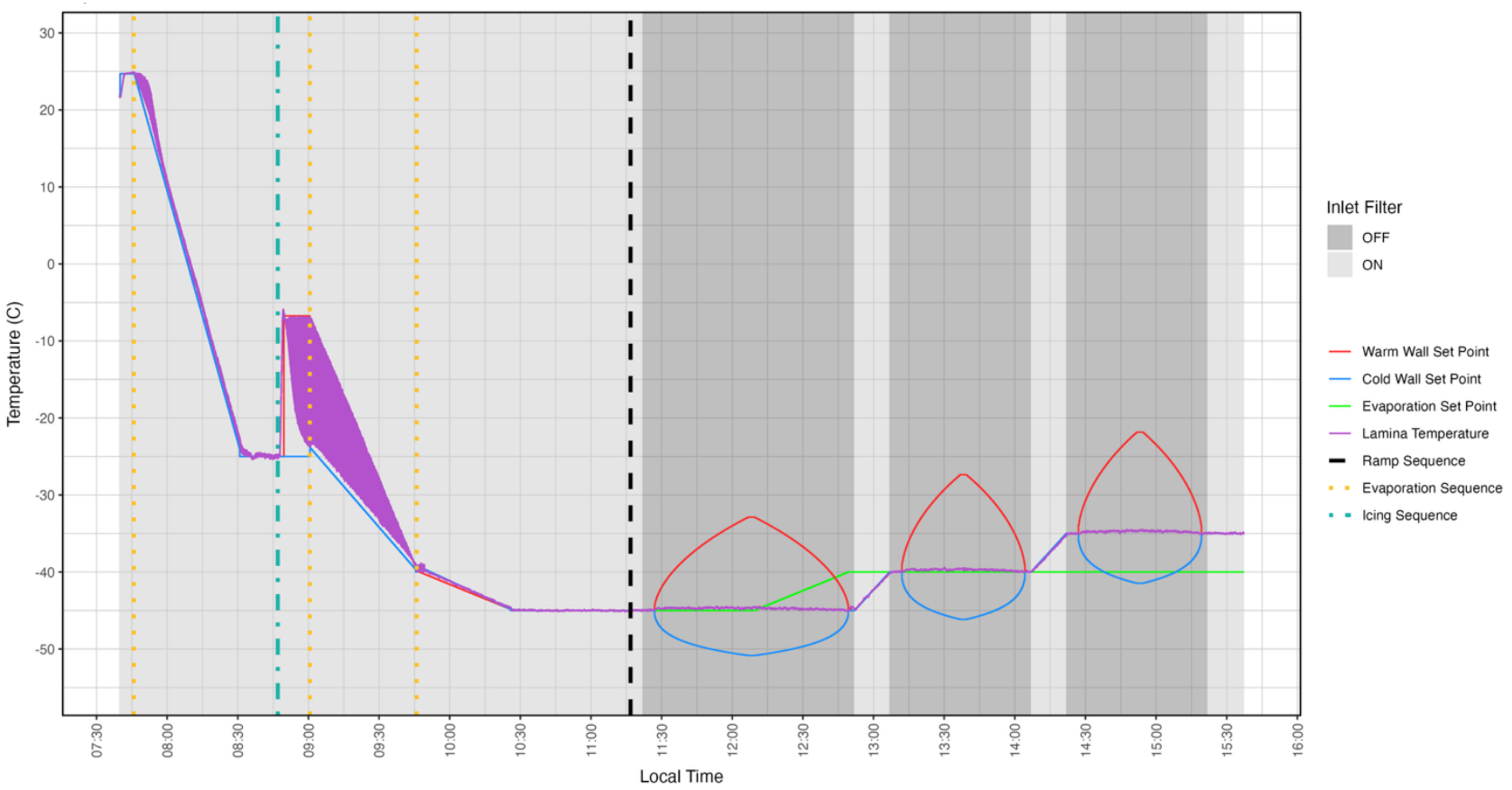

Figure S9 – Example ramp overview summary for the SPIN experiments conducted.

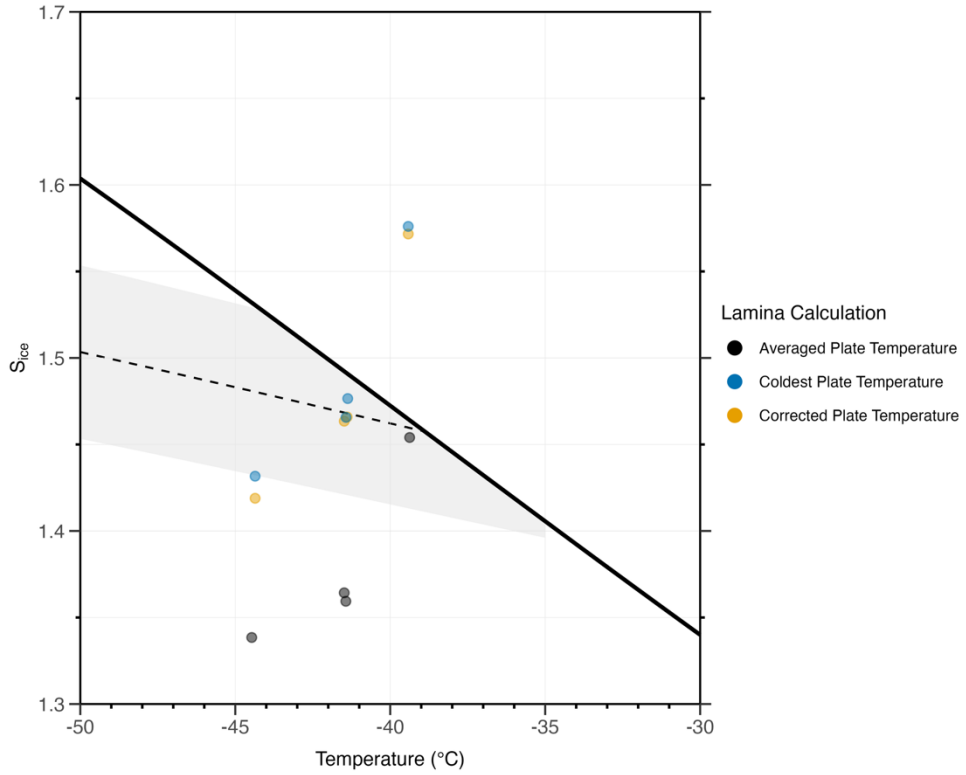

Figure S10 – Experimental ice onsets for calibration experiments using monodisperse (200 nm) ammonium nitrate aerosol.

Methods for onset quantification mirror the main text and panel lines/shading match those of Figs. S7 and S8. Colors indicate which thermocouple measurements were used in calculating the lamina S_{ice} for the SPIN. Lamina calculations follow pre-existing methods, see Garimella et al. (2016) and references therein. Averaged plate temperature uses the full plate, while coldest and corrected only use the coldest thermocouple measurements or average of several thermocouple measurements, respectively. In the latter two cases, lamina S_{ice} is calculated pairwise using the warm wall thermocouple at the same corresponding position. The authors note that all onsets depend strongly on refrigeration control values and other non-ideal lamina behaviour; these settings were actively tuned during calibration experiments to determine ideal operating values (i.e. those near -41.5°C).

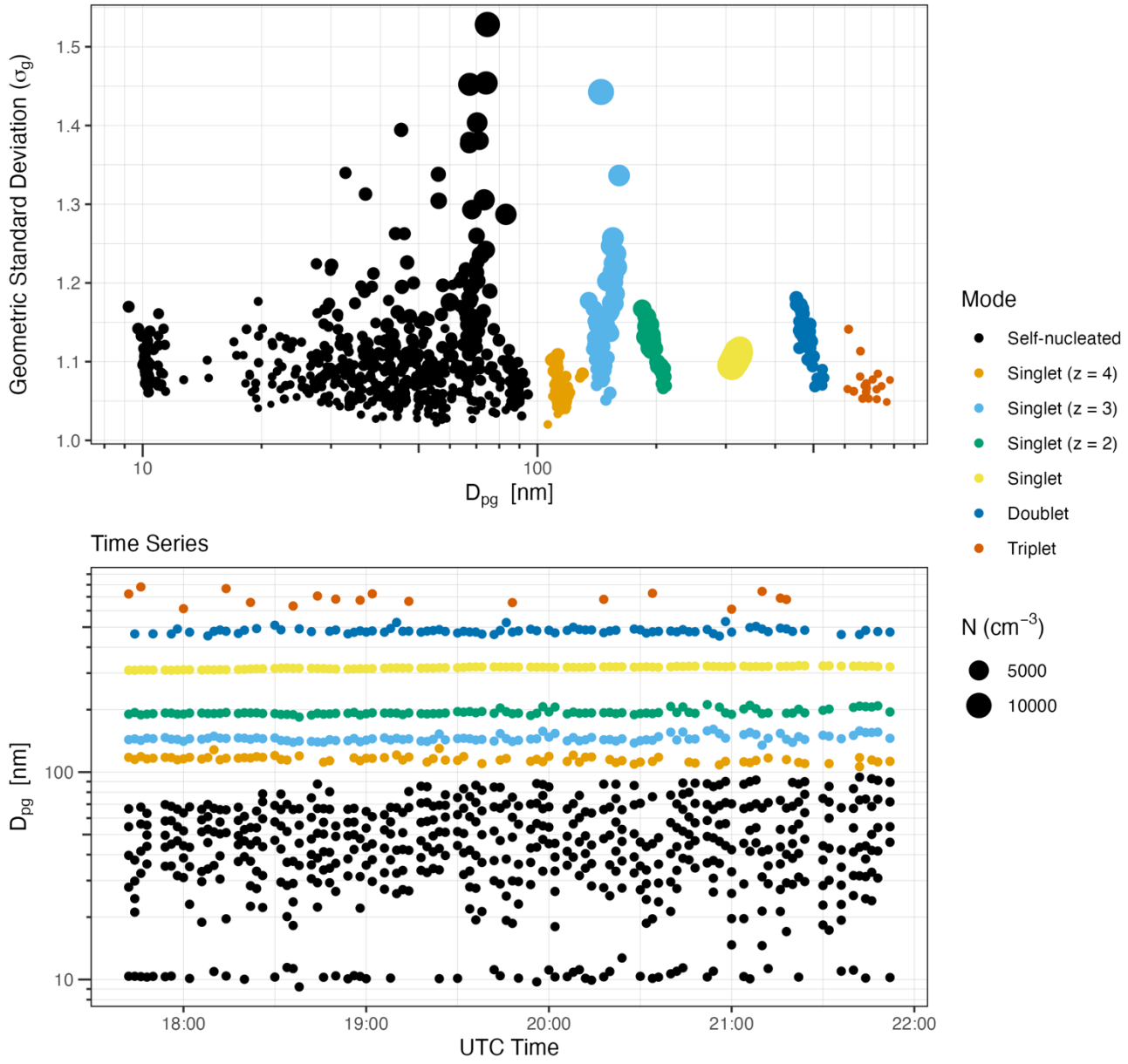

Figure S11 – Example multimodal output summarizing the lognormal parameters of limonene-AS BSOA particles

References

DeRieux, W.-S. W., Li, Y., Lin, P., Laskin, J., Laskin, A., Bertram, A. K., Nizkorodov, S. A., and Shiraiwa, M.: Predicting the glass transition temperature and viscosity of secondary organic material using molecular composition, Atmos. Chem. Phys., 18, 6331–6351, https://doi.org/10.5194/acp-18-6331-2018, 2018.

Froyd, K. D., Murphy, D. M., Sanford, T. J., Thomson, D. S., Wilson, J. C., Pfister, L., and Lait, L.: Aerosol composition of the tropical upper troposphere, Atmos. Chem. Phys., 9, 4363–4385, https://doi.org/10.5194/acp-9-4363-2009, 2009.

Garimella, S., Kristensen, T. B., Ignatius, K., Welti, A., Voigtländer, J., Kulkarni, G. R., Sagan, F., Kok, G. L., Dorsey, J., Nichman, L., Rothenberg, D. A., Rösch, M., Kirchgäßner, A. C. R., Ladkin, R., Wex, H., Wilson, T. W., Ladino, L. A., Abbatt, J. P. D., Stetzer, O., Lohmann, U., Stratmann, F., and Cziczo, D. J.: The SPectrometer for Ice Nuclei (SPIN): an instrument to investigate ice nucleation, Atmos. Meas. Tech., 9, 2781–2795, https://doi.org/10.5194/amt-9-2781-2016, 2016.

Koop, T., Luo, B., Tsias, A., and Peter, T.: Water activity as the determinant for homogeneous ice nucleation in aqueous solutions, Nature, 406, 611–614, https://doi.org/10.1038/35020537, 2000.

Li, Y., Day, D. A., Stark, H., Jimenez, J. L., and Shiraiwa, M.: Predictions of the glass transition temperature and viscosity of organic aerosols from volatility distributions, Atmos. Chem. Phys., 20, 8103–8122, https://doi.org/10.5194/acp-20-8103-2020, 2020.

Murphy, D. M., Cziczo, D. J., Froyd, K. D., Hudson, P. K., Matthew, B. M., Middlebrook, A. M., Peltier, R. E., Sullivan, A., Thomson, D. S., and Weber, R. J.: Single-particle mass spectrometry of tropospheric aerosol particles, J. Geophys. Res., 111, 2006JD007340, https://doi.org/10.1029/2006JD007340, 2006.

Niu, S., McCary, K. P., Alton, M., Krechmer, J. E., Stark, H., Surratt, J. D., Canagaratna, M., and Zhang, Y.: Simultaneously characterizing the volatility distribution and phase state of submicron secondary organic aerosols using a vocus vaporization inlet for aerosols with a chemical ionization mass spectrometer, ACS ES&T Air, acsestair.5c00155, https://doi.org/10.1021/acsestair.5c00155, 2025.

Rapp, C. N., Carrillo-Cardenas, G., Hussein, T., Niu, S., Zhang, Y., Brechtel, F. J., Hallar, A. G., and Cziczo, D. J.: Curve fitting algorithm for multimodal particle size distributions – a theoretical basis, Atmos. Meas. Tech., 19, 5373–5385, https://doi.org/10.5194/amt-19-5373-2026, 2026.

Zhang, Y., Nichman, L., Spencer, P., Jung, J. I., Lee, A., Heffernan, B. K., Gold, A., Zhang, Z., Chen, Y., Canagaratna, M. R., Jayne, J. T., Worsnop, D. R., Onasch, T. B., Surratt, J. D., Chandler, D., Davidovits, P., and Kolb, C. E.: The Cooling Rate- and Volatility-Dependent Glass-Forming Properties of Organic Aerosols Measured by Broadband Dielectric Spectroscopy, Environ. Sci. Technol., 53, 12366–12378, https://doi.org/10.1021/acs.est.9b03317, 2019.